TÜBİTAK

Turkish Journal of Earth Sciences

http://journals.tubitak.gov.tr/earth/

Research Article

Turkish J Earth Sci
(2023) 32: 275-293

doi:10.55730/1300-0985.1844

Contemporary velocity field for Turkey inferred from combination of a dense network of long term GNSS observations

Ali İhsan KURT[1], Ali Değer ÖZBAKIR[2,*], Ayhan CİNGÖZ[1], Semih ERGİNTAV[3], Uğur DOĞAN[4], Seda ÖZARPACI[4]

[1]General Directorate of Mapping, Geodesy Department, Ankara, Turkey
[2]Boğaziçi University, Kandilli Observatory and Earthquake Research Institute, Department of Geophysics, İstanbul, Turkey
[3]Boğaziçi University, Kandilli Observatory and Earthquake Research Institute, Department of Geodesy, İstanbul, Turkey
[4]Yıldız Technical University, Faculty of Civil Engineering, Department of Geomatic Engineering, İstanbul, Turkey

Received: 22.03.2022 • **Accepted/Published Online:** 07.10.2022 • **Final Version:** 28.04.2023

Abstract: The Anatolia–Aegean domain represents a broad plate boundary zone, with the deformation accommodated by major faults bounding quasi-low deforming units. First-order features of this deformation were obtained in the form of a GNSS-derived velocity field. During the last decade, the accuracy of velocity solutions was improved, and the expansion of continuous networks increased spatial resolution. Nonetheless, an accurate representation of the deformation field requires interstation distances much lower than the locking depth of nearby faults, which has not yet been satisfied. The basis for creating a precise and accurate velocity field is uniform processing of the time series recorded both in the campaign and permanent GNSS stations, at once and for a single reference system. Although for Anatolia the data density has increased 6-fold since the landmark work of Reilinger et al. (2006), this crucial integration has not been made. We aim to fill this gap by analyzing the data and providing a uniform velocity solution. In this study, we processed the time series of 836 stations, of which 178 are published for the first time. With a period of up to 28 years, we present the most accurate velocity field with increased spatial and temporal resolution and homogeneity. We used the improved coverage of the velocity field to calculate strain accumulation on the North and East Anatolian Faults. Modelled slip rates vary between 20 and 26 mm/yr and 9.7 and 11 mm/yr for the North and East Anatolian faults, respectively. The data can better constrain the kinematics of continental deformation, provide accurate boundary conditions for dynamic models, and help test outstanding hypotheses about the kinematics of the Anatolia-Aegean domain.

Key words: GNSS, data analysis, velocity field, strain accumulation, Turkey

1. Introduction

GNSS revolutionized active tectonics research by providing quantitative constraints on the mechanics of the continental lithosphere (Thatcher, 2009). Much research in recent years has focused on collecting or processing GNSS-derived velocity data for Turkey and the surrounding region (e.g., McClusky et al. 2000; Reilinger et al., 2006; Kreemer et al., 2014). These data have been instrumental in addressing principle debates of tectonics such as the relative importance of buoyancy and tectonic forces (Özeren and Holt, 2010), the link between mantle convection and surface deformation (Faccenna and Becker, 2010); studying the evolution of fault zone coupling (Özbey et al., 2021) as well as modelling the strain accumulation on major fault and interpreting locked and creeping segments (McClusky et al. 2000; Reilinger et al. 2006; Çakir et al., 2012; Ergintav et al. 2014). Furthermore, there is a growing application of radar imaging for fault kinematics analysis (e.g., Cavalié and Jonsson, 2014; Walters et al., 2014; Cakir et al., 2014; Bletery et al., 2020), which is calibrated by the GNSS velocity field and thus critically depend on the accuracy of GNSS data. Particularly important in this region is the characterization of seismic hazards in the North Anatolian Fault (NAF) and the East Anatolian Fault (EAF) zones.

Two very critical parameters for earthquake hazard assessment are strain rate and moment accumulation rate, both of which depend on the effective thickness of the zone of interseismic strain accumulation, i.e. the locking depth (Savage and Burford, 1973; Bird et al. 2015; Wei et al. 2010; Smith-Konter et al., 2011). Elastic dislocation theory provides a quantitative way of estimating locking depth, via the equation

$$v(x) = \frac{V}{\pi} tan^{-1}\left(\frac{x}{D}\right)$$

* Correspondence: ali.ozbakir@boun.edu.tr

where v is the fault-parallel displacement, V is the far-field (or secular) velocity, x is the fault-perpendicular distance, and D is the locking depth (Savage and Burford, 1973; for a study relevant to the study area, see Vernant, 2015). According to Smith-Konter et al. (2011), far-field velocity can be sufficiently represented if GNSS velocities are available at $x > 4D$. Moreover, to be able to invert the locking depth, and to sufficiently capture the gradient of the arctangent function at the origin, a high density of GNSS velocities at $x \leq D/2$ distances are required. For the NAF (and EAF), hypocentral depths indicate a mean locking depth of 15 km, requiring sufficient GNSS Station density within <7.5 km and >60 km perpendicular distance to the fault zone (for similar arguments for San Andreas Fault system, see Haines et al. 2015). Available GNSS station density from the most up-to-date velocity field (Figure 1; Kreemer et al., 2014) is ~46 km for the extent of the study area. Therefore, the available GNSS station density does not satisfy this range adequately.

The problems of active tectonics often require spatial extent or station density beyond what a single GNSS data network can provide. GNSS time-series can improve spatial resolution to better determine the deformation. The basis of obtaining a velocity field is to solve the coordinate time series acquired from the campaign and permanent GNSS stations. After removing outlier observations from the time series, all the solutions are combined to get the velocities of each site. The incremental nature of GNSS data ensures increased precision and accuracy (Nocquet, 2012), with accumulating data either in the form of extended time series or new campaigns elsewhere. To achieve this, it is necessary to combine individual GNSS time series or velocity solutions. The combination is done either as a result of using a homogeneous data analysis strategy using time series data or typically with a 7-parameter Helmert transform. The latter method is preferred because of inaccessible time-series data or the complexity of the process. However, the combination of velocities with those already published is often imperfect and introduces errors to the final solution owing to several reasons: (1) different assumptions and processing procedures/software, (2) uncertain or suspicious datum, (3) uncorrected earthquake cycle effect, (4) inadequate data acquisition/datum in campaign sites, (5) variety of reference frames. Therefore, the gold standard is the uniform processing of GNSS time-series with the same strategies at a time and for a single reference system (e.g., Nocquet, 2012).

In this study, we analyzed new GNSS observations at 186 sites in addition to data used by Kurt et al. (2020) through homogeneous processing of time-series for a single reference system, for the year 2020 and reestimated the velocity field from 836 sites with an average inter-station distance of 37 km. Furthermore, we calculated slip-rates of the NAF and EAF, with increased near- and far-field velocity estimates.

2. GNSS data

Previous GNSS observations incorporated in this study can be grouped according to their geographical extent. Region-wide datasets described the first-order features of regional kinematics, such as the westwards motion of Anatolia relative to the Eurasia-fixed reference frame, from the Bitlis-Zagros collision towards the Hellenic subduction zone, and an increase in the velocity from east to west in a counter-clockwise pattern around a pivot in Cyprus (McClusky et al., 2000; Reilinger et al., 2006). Subsequent studies focused on certain tectonic structures, seismically active fault systems or deformations in a regional base (Ayhan et al., 2002; Aktug et al., 2009, 2013, 2015; Ozener et al., 2010; Aktuğ and Kılıçoğlu, 2006; Yavasoglu et al., 2011; Reilinger and McClusky, 2011; Tatar et al., 2012; Tiryakioglu et al., 2013; Ozener et al., 2013a, 2013b, 2013c; Ergintav et al., 2014, Dogru et al., 2014; Aktug et al., 2016). The observational period and station distribution of these studies are summarized in Figure 1. Increasing epoch numbers at overlapping stations provides a great opportunity for more precise velocity estimations.

In 1997, the General Directorate of Mapping (GDM) started a new project to unify the GNSS velocity field and The Turkish National Fundamental GPS Network (TNFGN) was established with 594 homogeneously distributed sites between 1997–1999, to realize a three-dimensional modern nationwide reference coordinate system. As the permanent GNSS stations concept has become widespread in the upcoming years, it has improved the temporal and spatial coverage of sites having GNSS observations all over the country. Now, the Turkish Real-Time Kinematic GNSS Network (CORS-TR; 158 stations), the Turkish National Permanent GNSS Network (TNPGN; 19 stations), and Marmara Region Continuous Network (MAGNET; 11 stations) provide a continuous flow of GNSS data. Kurt et al. (2020) reprocessed all GNSS data of TNFGN, TNPGN, CORS-TR, and MAGNET between 1992 and 2019 using a homogeneous data analysis strategy, updated satellite orbits and Earth Orientation Parameters increasing the number of sites by %30 compared to Aktug et al. (2011).

The data set used in this study consists of %78 campaign type sites and %22 continuous stations and covers the period between 1992 and 2020. The session length of the campaign type observations is between 7–10 h while permanent stations provide 24 h of data.

The main contribution of campaign data comes from the TNFGN (Ayhan et al, 2002a), which has operated for a considerable period of nearly 20 years. The network points having an inter-station spacing of about 15–65 km were also collocated at some points of the Turkish

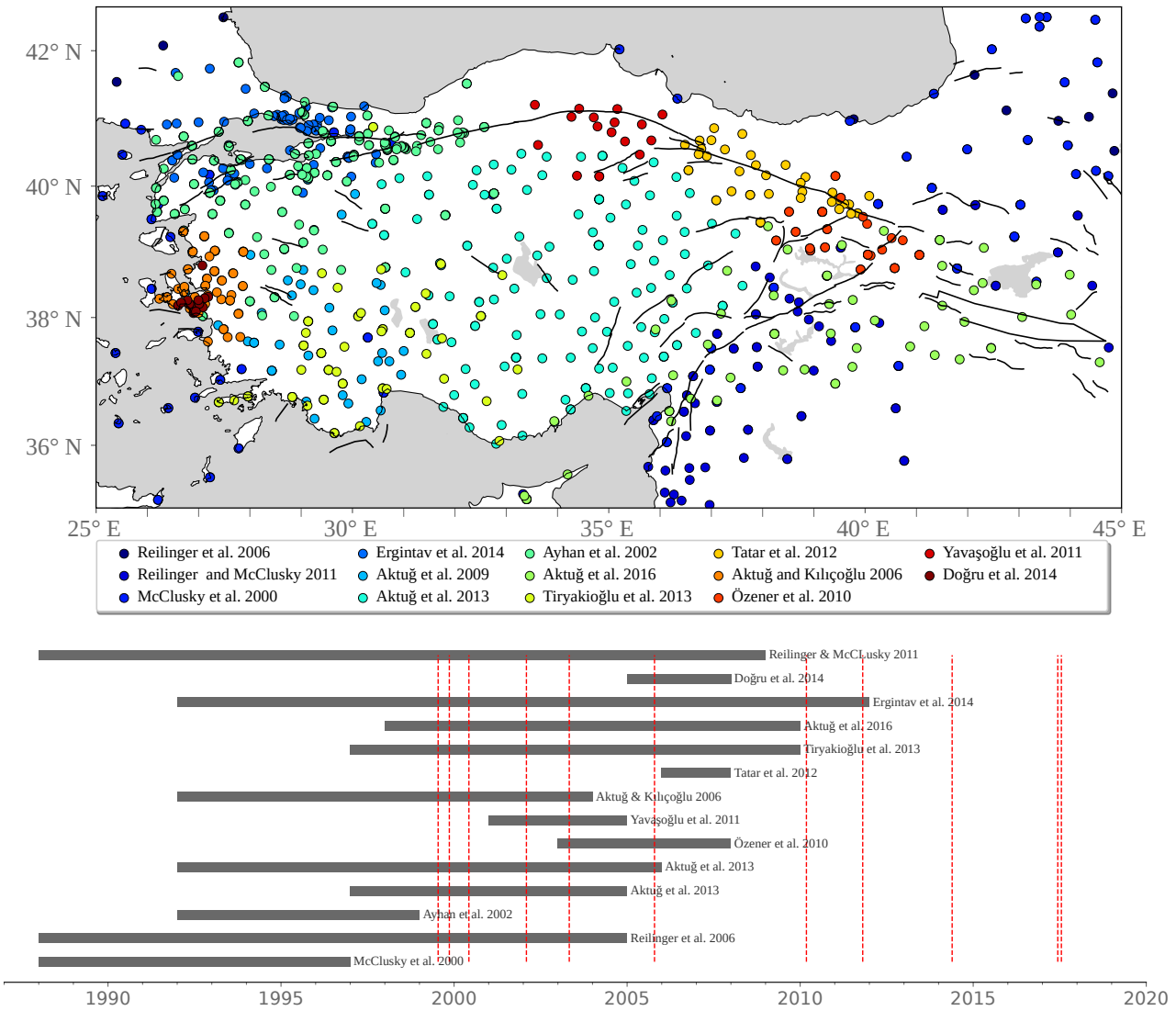

Figure 1. (top) GNSS studies published in the literature. For clarity, studies that have few sites and small spatial coverage are omitted. (bottom) The observation periods of previous GNSS studies. M > 6 earthquakes are shown with vertical red dashed lines, whose source information is given in Kurt et al. (2020).

National Horizontal Control Network and Vertical Control Network. Geodynamic sites and tide gauge GNSS benchmarks, installed and maintained by the General Directorate of Mapping, are also included in this study to improve spatial resolution. We incorporated the CORS-TR nationwide network with ~100 km spacing and some of the stations operated by TÜBİTAK Marmara Research Center (MAGNET), Bursa Water and Sewerage Administration General Directorate (BUSKİ), Sakarya Water and Sewerage Administration General Directorate (SASKİ), and İstanbul Water and Sewerage Administration General Directorate continuous (İSKİ) GNSS networks to fill the gaps.

Blewitt and Lavalle (2002) showed that for tectonic studies or reference frame production, a minimum 2.5-year observation period would eliminate velocity bias. Therefore, we adopted this criterion for the time series. In the campaign type GNSS data, the minimum and maximum periods are 2.7 and 28 years respectively. In terms of continuous GNSS station data, the minimum and maximum observation durations are 2.1 and 17.1 years respectively. Two permanent stations having a 2.1-year observation period with weighted root mean square error (wrms) below 1 mm are also included in the data set. The velocities of those stations are compliant with the velocities of their neighboring sites.

At the beginning of the velocity field determination, we evaluated 1303 sites having a minimum of 2 epochs surveyed coming from the combination of all campaign and continuous site solutions. Some of the sites are influenced by postseismic effects in the form of displacement offsets.

So, postseismic periods are removed from those time series. At sites having coseismic slips due to earthquakes, we decided which part to use considering the data span before and after the earthquake. Some sites had stability inconsistencies due to weak bracing into the ground, instrumental malfunctions, observational blunders or some local impacts. We removed those sites according to their time series resulting in large wrms values or through cross-validation tests with their neighboring stations. By examining the daily coordinate time series of each site in detail, attention has been paid to representing the velocity field of the region most accurately. The distribution of the data used in this study is summarized in Table 1 and presented in Figure 2.

We calculated inter-station distances of the sites from Delaunay triangulation and nearest-neighbor analysis. Figure 3 shows the histogram of interstation distances of 836 sites with an average distance of 37 km.

Figure 4 shows the distribution of epoch numbers of sites and the observation durations for campaign type observations. As can be seen, it is not uniform in time, especially, this is important during the combination of them within the active tectonic regime. In other words, some of them were affected by different earthquakes and, their analyses could be realized to isolate the short-term deformation anomalies (earthquakes, postseismic motions, subsidences etc.) in time, systematically. The information about the epoch and time intervals of all sites is given in Supplementary Table 2.

3. Methods

3.1. GNSS data processing and combination

GNSS data were processed and uncertainties were estimated with the GAMIT/GLOBK software package (Release 10.70; Herring et. al., 2018), using standard techniques described in Reilinger et al. (2006). Data Analysis Strategy is summarized in Table 2.

While long-term GNSS campaigns are divided into 15-day sections, daily permanent station solutions are combined monthly. A total of 483 solution files (227 campaign and 256 permanent stations solutions) between 1992 and 2020 were combined and a final solution was achieved. The GLOBK (Global Kalman Filtering) module of the GAMIT-GLOBK (V10.70) software is used to combine the campaign solutions. Campaigns with very close dates or campaigns having the same observation dates are combined at the GLOBK stage.

At first, high a priori variance (±100 m) is defined for all sites and the loosely constrained solution was obtained by the Kalman Filtering technique (Herring et al., 2018). Later, to define the reference frame with the loosely constrained solution, a Helmert transformation with 12 parameters (3 translation, 3 rotation, 3 translation velocity, and 3 rotation velocity) is applied between the ITRF2014 (Altamimi et al., 2016) coordinates and velocities of 33 IGS stations included in the analysis (Figure 5). Previous studies generally used 10-20 IGS stations for datum definition. In this study, we used 33 IGS sites to increase redundancy and to obtain a more stable datum definition. The ITRF2014 coordinate and velocity field is obtained from the "igb14_comb.apr" file (Herring et al., 2018), where the ITRF, IGS, EPN, and NGS solutions were combined to realize ITRF2014 (the most recent update, MIT). This coordinate file is a combined coordinate and velocity list of the solutions of global and regional GNSS stations published by the above-mentioned institutions based on ITRF2014. Finally, the loosely constrained solution consisting of all campaigns is adjusted in the ITRF2014 datum with minimum constraints on the coordinates and velocities of 33 IGS stations. Statistics of the combination are presented in Table 3.

Table 1. Data sources and number of sites used in this study.

Data Source	Number of Sites
Turkish National Fundamental GNSS Network (TNFGN)	608
Turkish Real-Time Kinematic GNSS Network (CORS-TR)	134
Campaign Sites, other	30
Turkish National Permanent GNSS Network (TNPGN)	20
TÜBİTAK Marmara Region Continuous Network (MAGNET)	10
Turkish National Sea Level Monitoring System (Tide Gauge Sites)	12
Bursa Metropolitan Municipality Water and Sewerage Administration (BUSKİ)	6
General Directorate of Sakarya Water and Sewerage Administration (SASKİ)	6
İstanbul Metropolitan Municipality Water and Sewerage Administration (İSKİ)	5
International GNSS Service (IGS)	5
Total	836

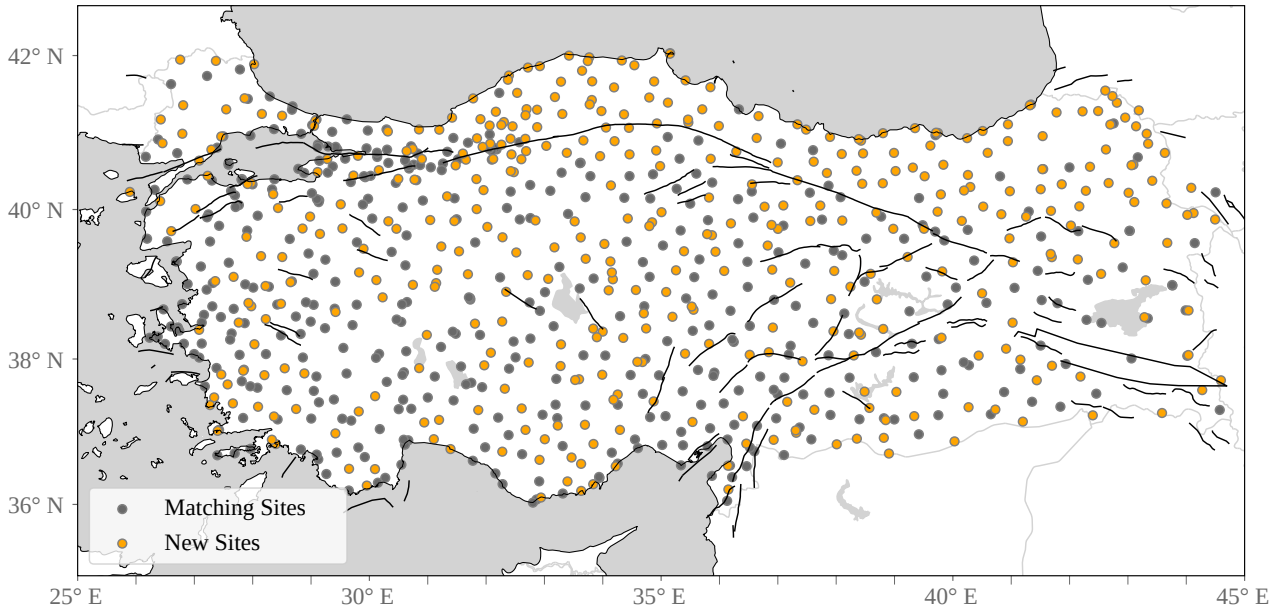

Figure 2. GNSS stations used in this study (The velocity solutions are given in Supplementary Table 1). Stations shown in orange are the new stations whose velocities are reported for the first time in this study, whereas black circles are the ones reported in previous studies.

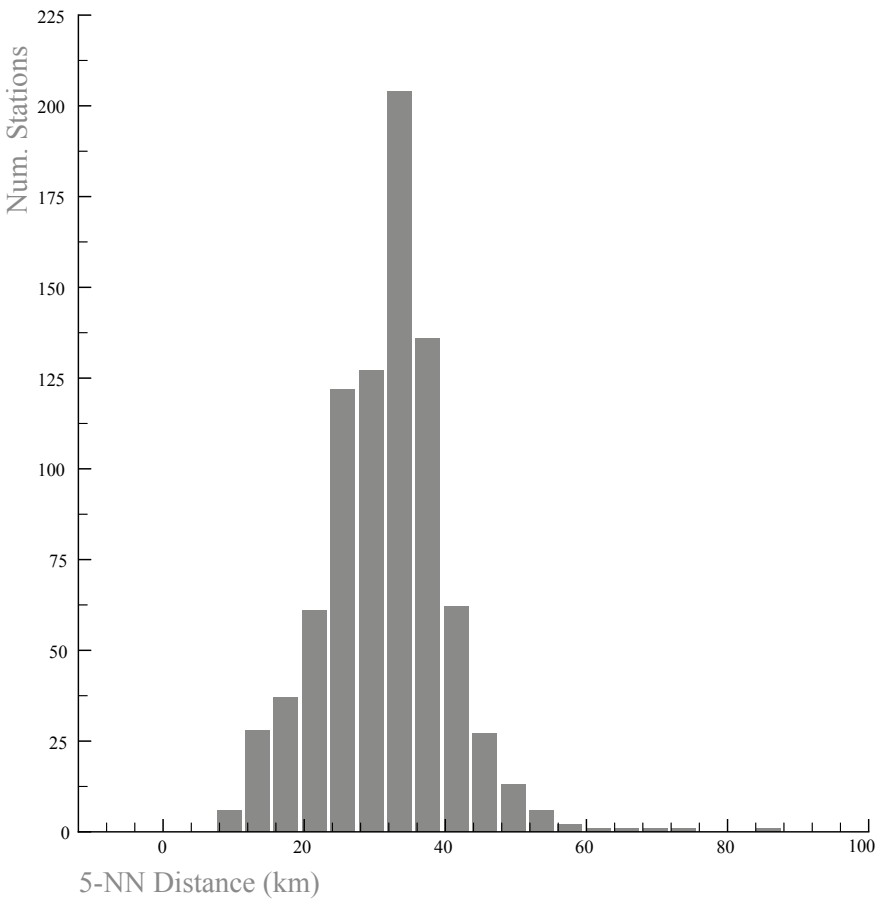

Figure 3. The histogram of inter-station distance, calculated based on the average pairwise distance for 5-Nearest Neighboring stations, for all the sites used in this study.

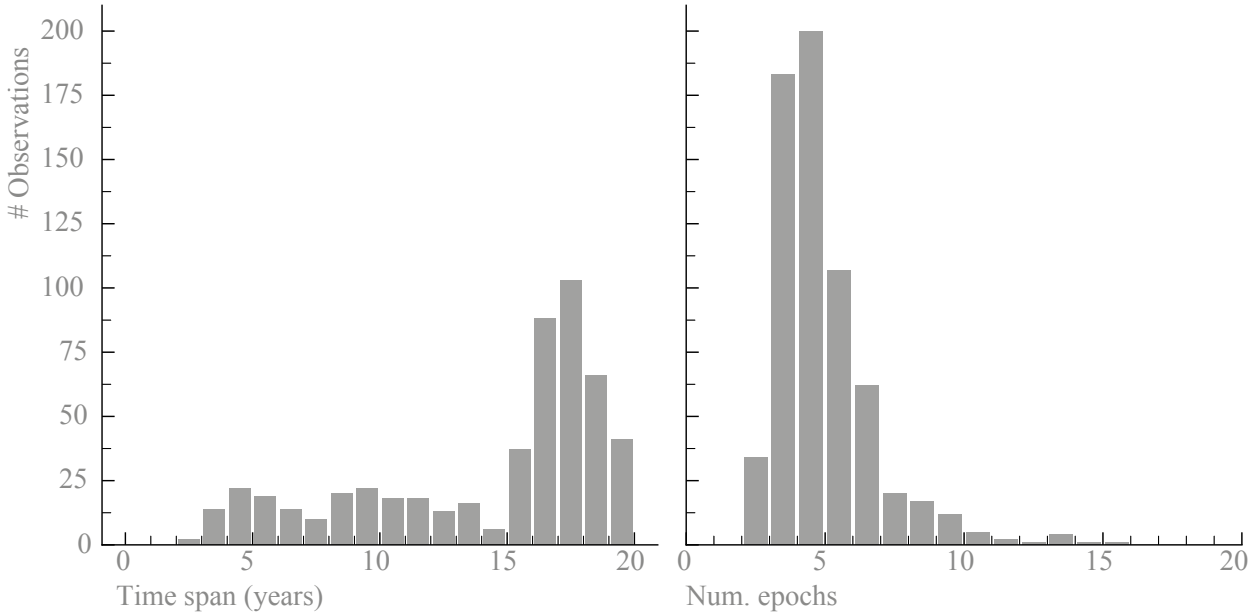

Figure 4. Distribution of period and number of epochs for campaign sites used in this study.

Table 2. Data analysis strategy.

Software	GAMIT/GLOBK V10.70
Observations	Double differenced phase
Orbits	IGS final repro2 SP3's
Elevation cut-off angle	3 degrees
Earth Orientation Parameters	USNO bulletin b
Tropospheric Mapping Function	Vienna (VMF1)
A Priori Troposphere Model	gpt2_5.grd (global pressure temperature)
Tropospheric Delay Parameters Interval	2 h
Ocean Loading	otl_FES2004.grid
Atmospheric Loading (tidal)	ANU100826_grid.atl (grid)
Atmospheric Loading (nontidal)	atmfilt_cm.YYYY (grid)
Magnetic Model	IGRF12
Number of IGS stations included	33 stations
Antenna Phase Center Correction	Absolute (IGS14)
Reference Frame Stabilization	ITRF2014 (igb14_comb.apr, igb14_comb.eq)

3.2. Velocity field in Eurasia plate fixed reference frame

No-net-rotation in which the surface integral of angular velocity is zero, is usually used as the constraint on defining a terrestrial reference frame in the presence of plate tectonics. ITRF velocities are defined with respect to the no-net-rotation and NUVEL-1A model and since ITRF2000 was initially aligned to the global NNR-NUVEL-1A which also satisfies that condition (Altamimi et al., 2017). In practice, the ITRF2000 orientation time evolution was defined by minimizing its 3 rotation rates with respect to the NNR-NUVEL-1A plate motion model using the horizontal velocities of a polyhedron of core ITRF sites (Kreemer et al. 2006).

It is more informative for crustal deformation studies to view the velocities in a plate-fixed reference frame such as Eurasia rather than viewing the velocities in a reference frame such as ITRF2014.

Different approaches for defining a plate-fixed reference frame may produce consistent velocity fields and they may be sufficient enough to analyze tectonic deformation over

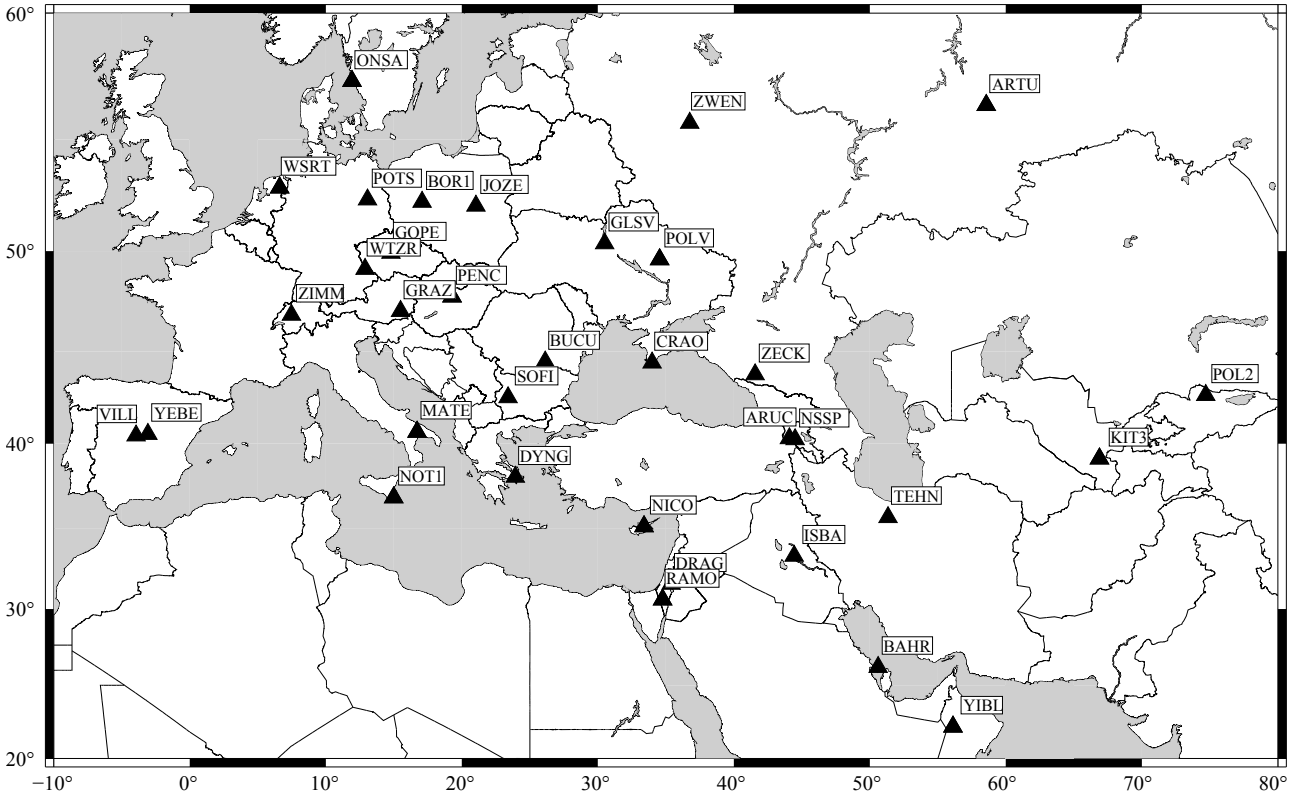

Figure 5. IGS stations used in the analysis.

Table 3. Statistics of the adjustment (N: North, E: East, U: Up components).

Positional Statistics (WRMS)	N E U	0.76 mm 1.04 mm 3.20 mm
Velocity Statistics (WRMS)	V_N V_E V_U	0.31 mm/year 0.20 mm/year 0.46 mm/year
RMS of Reference Station Coordinates		2.00 mm
RMS of Reference Station Velocities		0.57 mm/year

a region. But combining velocities from different studies requires caution because of the bias coming from different reference frame definitions. To compare or combine velocities from different sources, it is highly recommended to use the same strategy as the previous results or make appropriate transformations between the velocity fields.

In this study, to estimate velocities in a Eurasia plate fixed reference frame, we used residual velocities of 33 IGS sites given in (Herring et al., 2018) derived from relative to Eurasia plate as defined by (Altamimi et al., 2017) ITRF2014 plate motion model. The rotation vectors are estimated by GAMIT/GLOBK software. The relative rotation vector (Euler Pole) of Anatolia with respect to Eurasia with is given in Table 4, together with other published estimates.

After defining the plates, the Euler Pole is determined by selecting a set of stations in Anatolia and a set of stations in Eurasia homogeneously distributed. For the stability of the rotation vector, only continuous stations are used on both plates. As seen in Table 4 the 1-sigma uncertainties are lower than in the other studies.

4. Results and analysis

The velocity solution of the uniform processing of time-series with respect to the Eurasia-fixed reference frame is plotted in Figure 6 and given in Supplementary Table 1 with their associated standard deviations along with their relative correlations. While the realistic uncertainties of the velocity solutions were on the order of <1 mm/y, the post-fit RMS of reference frame sites were found to be ±2.0 mm and ±0.57 mm/yr for coordinates and velocities respectively.

The overall pattern in the velocity solution is in agreement with the previous solutions (e.g., Aktug et al., 2009; Kreemer et al. 2014), however, there are statistically significant deviations for overlapping stations (Supplementary Figure 1). This is due to the increased

Table 4. Euler vector of Anatolia relative to Eurasia and 1 sigma uncertainties.

Longitude °E	σ_E	Latitude °N	σ_N	Rate deg/Myr	σ_R	References
32.6	0.4	30.8	0.8	1.2	0.1	McClusky et al. (2000)
32.1	0.7	30.8	0.8	1.231	0.023	Reilinger et al. (2006)
32.643	0.004	26.880	0.017	0.84	0.001	This Study

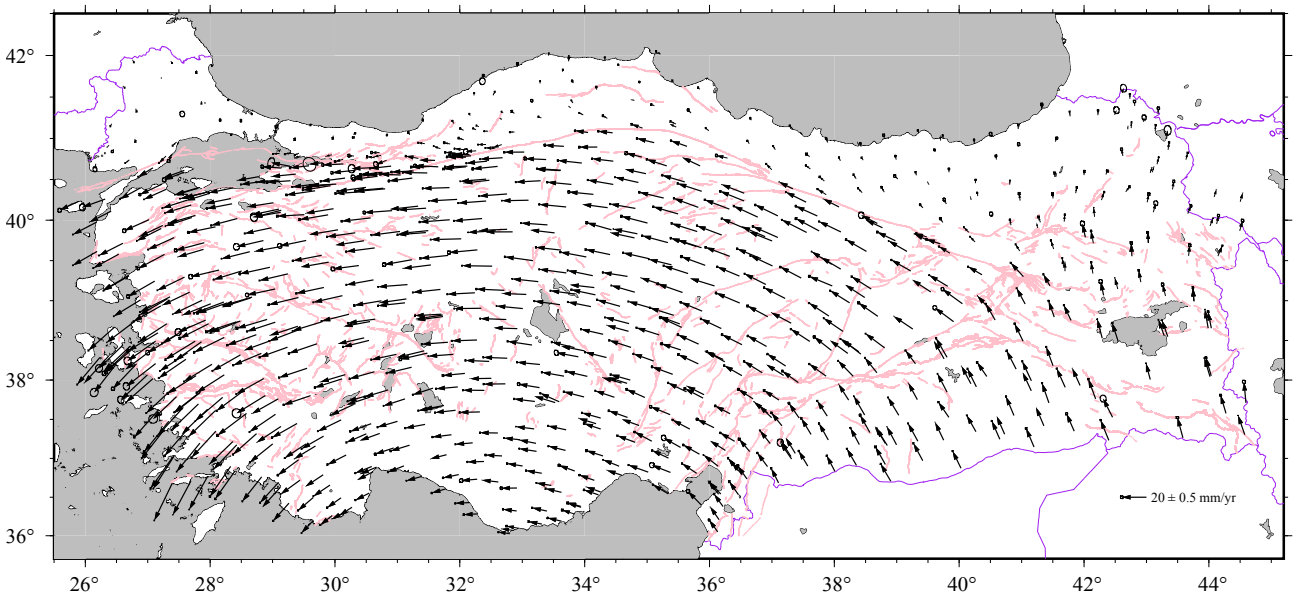

Figure 6. The final velocity solution in the Eurasia-fixed reference frame (with 95% confidence ellipses). The data is tabulated in Supplementary Table I.

length of time series employed in our study. To better highlight the differences in our solution we interpolated the velocity solution into a regular 0.1° × 0.1° grid using splines (gmt gpsgridder; Wessel et al. 2019). We assume that the global model of Kreemer et al. (2014) provides a combination of the most up-to-date velocity solutions and has a good spatial coverage extending beyond the geographical focus of this paper. Figure 7 shows the difference between this study and Kreemer et al. (2014) for east and west components of the gridded velocity field (Figure 7A), as well as common sites (Figure 7B). There is an apparent misfit of >3 mm/y in the vicinity of NAF, locally reaching 5 mm/y. This result is most likely due to increased sampling of the near-fault region surrounding the NAF (see the next subsection; and Figure 9).

The differences in the north component are mostly localized in a large zone of central Anatolia, the easternmost part of NAF, and the southeastern part of the Sea of Marmara. The anomaly in central Anatolia is rather prominent. The significant differences in N-component do not spatially correlate with those for E-component. But this is not surprising, as the N-components are rather small (Figure 6), and any improvement in the velocity estimates will result in large deviations. As the period of observation and station density for the central Anatolian stations increased dramatically, we could resolve better the velocities there.

We used the mean of pair-wise distances for the five nearest neighbors. We limited our analysis to the region enclosed by the national borders of Turkey. Therefore, we cropped Kreemer et al.'s (2014) data to have the same spatial limits. As seen in Figure 8 the spatial resolution of our model increased with decreasing interstation differences. Furthermore, the distribution looks more symmetrical, that is the number of outlier stations is significantly reduced.

Our study provides significantly improved coverage of the near-field and far-field around major faults. Near field and far-field are defined above as $x < D/2$ and $x > 4D$, respectively. This gives $x < 7.5$ km and $x > 60$ km for EAF and NAF. The upper bound for the far-field is taken to be 100 km. We report one more station velocity in addition to the existing five near-field stations for EAF (Figure 9a). Moreover, eight new station velocities are available

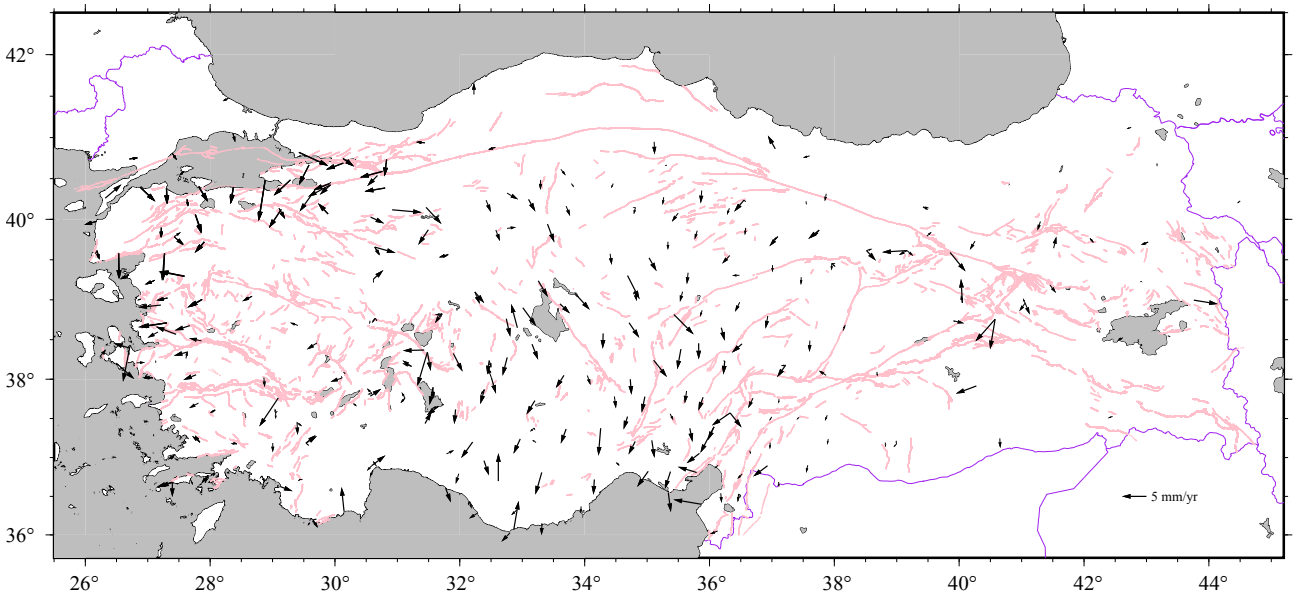

Figure 7A. The difference between the gridded N- and E-components of Kreemer et al. (2014) and this study.

in the far-field, in addition to 16 existing stations. For the NAF, 14 new velocity estimates are available in the near field and 44 new velocity estimates are available in the far-field (Figure 9b). As described below, these new estimates provide significant new constraints on the character of strain accumulation along the NAF and EAF.

4.1. Interseismic strain accumulation along NAF and EAF

Earthquake hazard analyses strongly depend on the spatial distribution of the strain accumulation rates along the active fault zones. Furthermore, the location, periodicity, and causes of aseismic creep are central to a quantitative seismic hazard assessment (see Avouac, 2015 for a review). Generally, the strain accumulation is modelled as dislocation in elastic half-space (Savage and Burford, 1973). There are two parameters in this problem: slip rate and locking depth. Locking depth controls the extent of the strain on the surface induced by loading at depth. To demonstrate the spatial resolution of the new GNSS-derived velocity field, we calculate strain accumulation over a series of profiles perpendicular to the East Anatolian Fault (EAF) and the North Anatolian Fault (NAF) (cf. Vernant, 2015 for a similar analysis carried out on the NAF and EAF).

Strain accumulation inverse models have been applied to the North Anatolian Fault (NAF) and East Anatolian Fault (EAF), as constrained by the then-available GNSS data (McClusky et al., 2000; Cakir et al., 2005; Reilinger et al., 2006; Çakir et al., 2012; Tatar et al., 2012; Aktug et al., 2013; Mahmoud et al., 2013; Cakir et al., 2014; Kreemer et al., 2014; Aktug et al., 2016; Aslan et al., 2019). In an inverse strain problem, the robustness of the solution critically depends on the observation capacity in the near field deformations (that is, determined by the locking depth) and the precise estimation of the far-field, often represented by the secular motions (e.g., the Euler pole). As shown in Figure 9, we significantly improved the number of near-fault observations and their accuracy with longer time series. Furthermore, the new data adequately samples far-field, thus it is often unnecessary to calculate relative motions for the far-field locations. Although ours is not an exhaustive analysis of strain accumulation, we show that the increased near-fault spatial coverage, precisions of far- and near-field observations and temporal span of GNSS time-series constrain the kinematics better in comparison to the previous studies (Table 5).

We chose two velocity models to demonstrate the improved spatial resolution of our model McClusky et al. (2000) and Kreemer et al. (2014), hereafter denoted by M2000 and K2014 respectively, instead of the many local studies. The regional model M2000 is restricted to pre-1999 time-series, hence free from the postseismic effects of Mw7.4 İzmit and Mw7.2 Düzce earthquakes. The global model K2014, on the other hand, provides a combination of post-1999 velocity solutions and has a good spatial coverage extending beyond the geographical focus of this paper. Therefore, such a comparison facilitates the discussion on the temporal evolution of strain, comparing the pre and posttimes of 1999 events (e.g., profile NAF 11, Figure 10), and demonstrates the superior spatial resolution of our data set, compared to the previous models.

Figure 10 (NAF) and Figure 11 (EAF) show the fault-parallel component of the velocity vectors from this study,

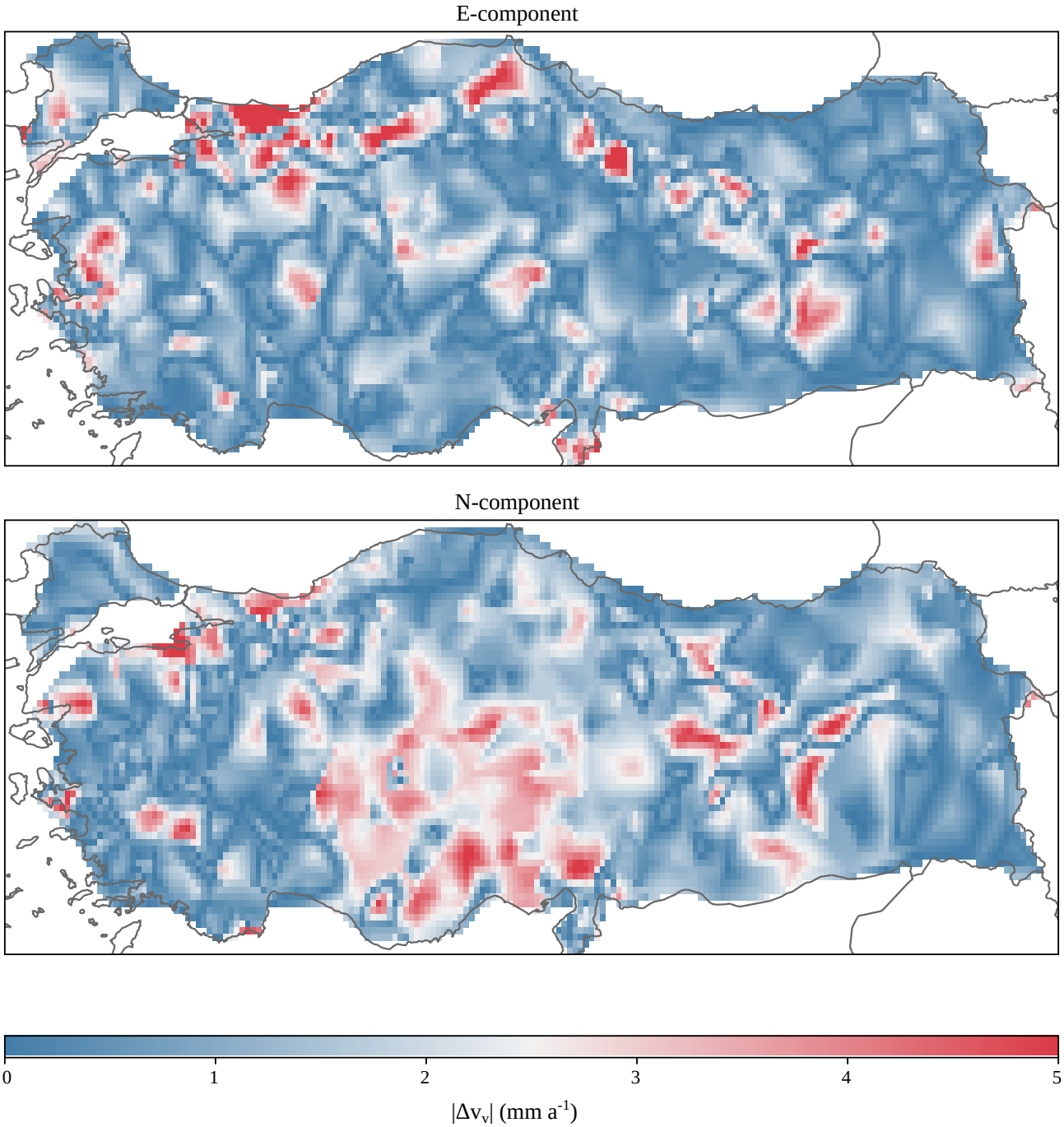

Figure 7B. The difference between the Kreemer et al. 2014 and this study for matching sites. Significant differences in the proximity of NAF and EAF suggest that the InSAR derived strain-rate field could be improved by using our solution.

superimposed by data points tabulated in M2000 and K2014. The NAF and EAF profiles are constructed by projecting velocity vectors within a swath of 50 km and 45 km, respectively (except Profile 12 (40 km) in Figure 10 to avoid overlapping with Profile 11 in Figure 10). The length of profiles is taken to be 120 km for NAF and 100 km for EAF, to incorporate sufficient near- and far-field data points. To apply the strain accumulation model (Savage and Burford, 1973), we fixed the locking depth to 16 km based on a homogeneous earthquake catalogue for Turkey (Tan, 2021) and focused on the variations of the strain accumulation rates, only. The deformation zone is estimated as twice the locking depth and depicted on all the profiles in Figures 10 and 11.

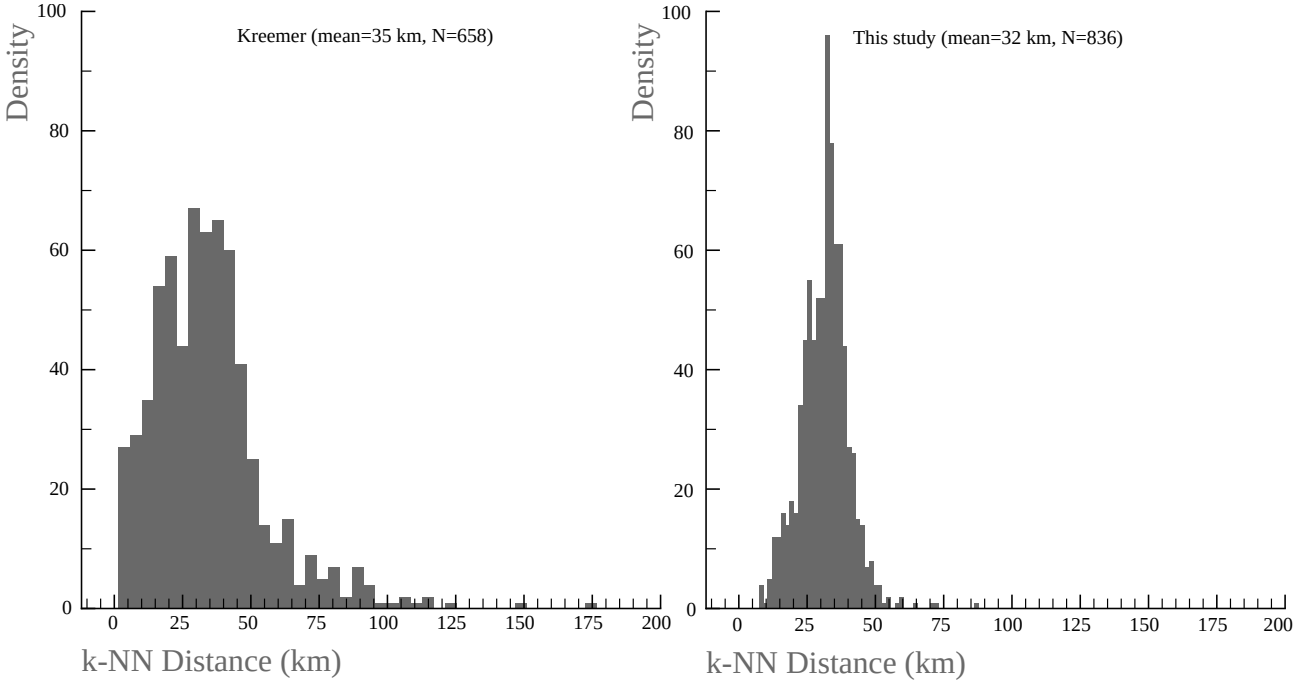

Figure 8. The histograms of inter-station distance, calculated based on the average pairwise distance for 5-Nearest Neighboring stations, **(a)** for Kreemer et al. (2014) stations, **(b)** for all the sites used in this study.

The main findings are listed below:

1. Figures 10 and 11 show the significant increase of data points compared to previously published velocities shown in Figure 1A, particularly for the deformation zone of EAF and the eastern half of the NAF. For example, profiles NAF01–07 include as much new data as (or more than) published (Figure 10).

2. The locked and creeping zones are identified. For example, if K2014 velocities were to be used then it would not be possible to resolve whether EAF is undergoing creep or not on profile EAF 1 (Figure 11, Bingol-Karlıova segment). On Profile EAF 02, (Figure 11, Palu segment), creep anomaly (Cavalié and Jonsson, 2014; Ergintav et al., 2018[1]) is clear with the support of high precision creepmeter measurements in the near field zone while K2014 controls the half part of the profile with highly scattering data sets.

3. The motion on the opposite sides of the faults beyond the deformation zone is adequately sampled, which was not available before (profiles NAF 01-10, Figure 10 on the Eurasian plate and profiles 02-05, Figure 11 on the Arabian plate). In the absence of these "blind" zones, previous strain models used Euler-pole constrained velocities to calculate the strain accumulation (Walters et al., 2014; Weiss et al., 2020; Bletery et al., 2020, Güvercin et al., 2022), which might not reflect the true nature of the fault kinematics.

4. Based on our velocity field, the slip rate increases from the east (20 ∓ 1 mm/yr) to the west (26 ∓ 1.1 mm/yr) along NAF–that is due to the increased rate of Anatolian motion towards the Hellenic Arc (McClusky et al., 2000). Similar results are presented in the literature (e.g., Reilienger et al., 2006, Özbakır et al., 2017), albeit the slip-rate variation is constrained by sparse data. Our data increase the spatial resolution in detail. Especially, new data in the near field (the profiles NAF 03-10, Figure 10) improve the spatial control in the near field dramatically. In previous studies, researchers tried to fill these gaps with imprecise PSInSAR data sets (Cakir et al., 2014). The standard deviation of this study is <1–1.5 mm/yr for these zones, whereas the published studies estimated three times larger standard deviations.

5. Along the EAF, the creeping segment seems to differentiate fault segments with uniform slip rates (The profiles EAF 03-05, Figure 11-Pütürge, Erkenek, Pazarcık segments) from the segment with elevated slip rates (The profile EAF 01, Figure 11). The creep on profile EAF 02 has been previously measured using in-situ creep meters (Ergintav et al., 2018, Palu segment), whose amplitude is thus corroborated with this study.

[1] Ergintav S, Çetin S, Selver S, Özdemir A, Çakır Z et al. (2018). New evidence for spatiotemporal fluctuations of slip rate on the East Anatolian Fault, Turkey from newly installed creep meters and seismological data. EGU General Assembly 2018. Geophysical Research Abstracts, Vol. 20, EGU2018-9395-1, 2018.

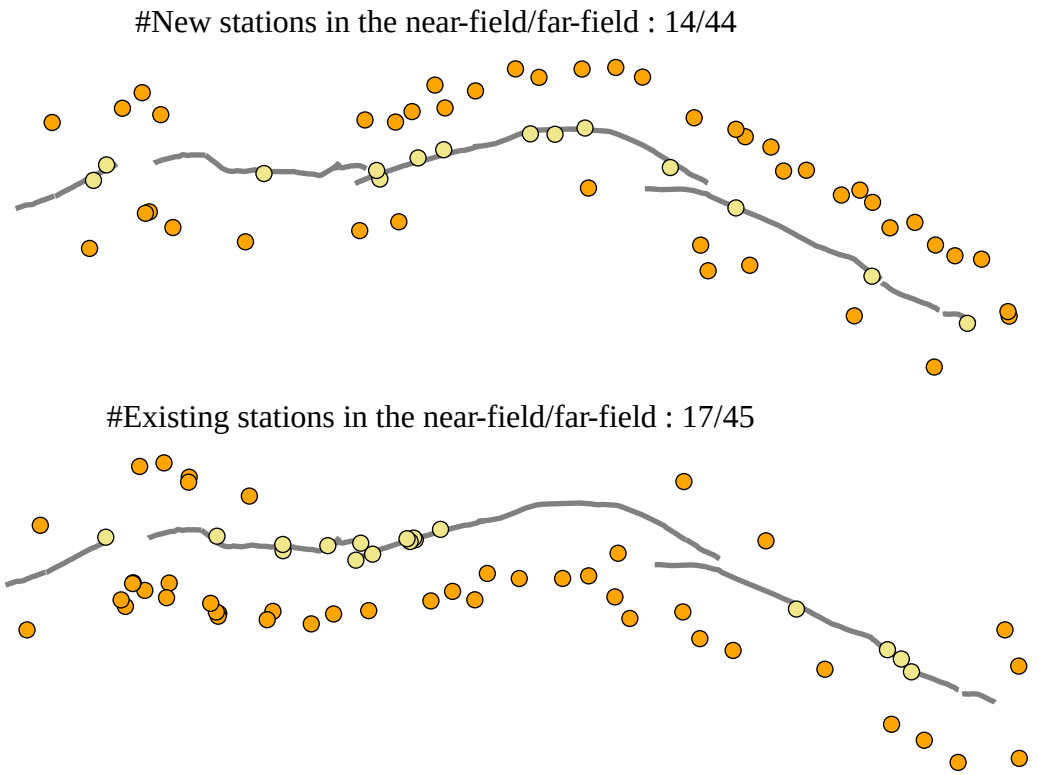

Figure 9A. The number of near- and far-field stations for the NAF.

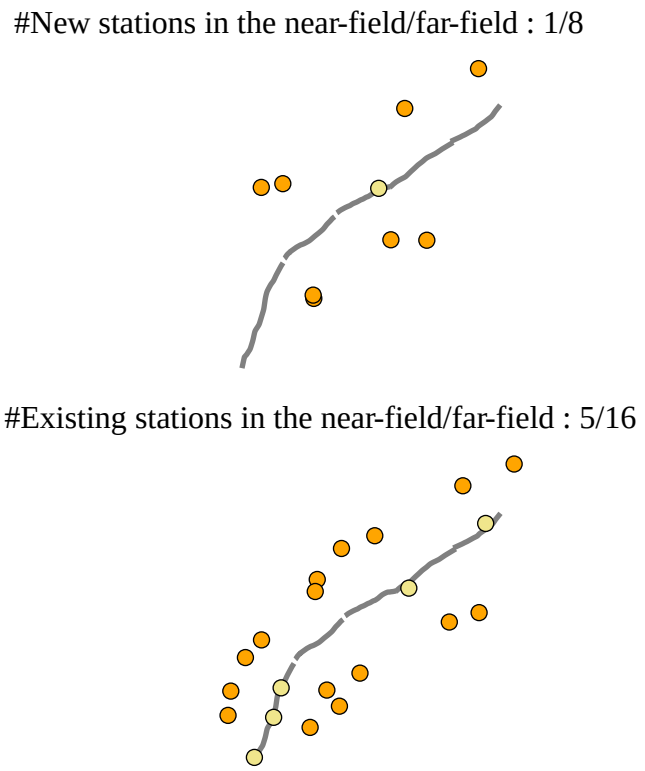

Figure 9B. The number of near- and far-field stations for the EAF.

Table 5. Average standard deviations of velocity fields.

σ_E	σ_N	References
1.529	1.467	McClusky et al. (2000)
1.030	0.949	Kreemer et al. (2014)
0.216	0.249	This Study

Published slip-rates for the EAF based on GNSS reports 9-10 mm/yr for the whole fault zone (McClusky et al., 2000; Reilienger et al., 2006) whereas Cavalie and Jonsson (2014) suggested ~13 mm/yr from InSAR. This difference comes from the contribution of the near field InSAR data (<5 km), along the Pütürge-Palu segment. The estimation of Cavalié and Jonsson (2014) was affected by the creep zone with their limited data sets and estimated higher than the mean value of the previous ones.

6. The section of NAF at İsmetpaşa is the typical example of a creeping fault, which has been repeatedly identified by the local GNSS campaigns and some local networks (e.g., Bilham et al., 2016, and the references therein). The creep is also resolved in profile NAF 09 (Figure 10), furthermore to the east we model creep in profile NAF 08 (Figure 10). The segment of NAF containing piercing points of both profiles corresponds to the surface rupture of the 1944 Ms7.2 Bolu-Gerede earthquake. Cetin et al. (2014) have previously resolved this creeping zone by using InSAR constrained slip model and suggested the creep is triggered by the 1944 earthquake. Thanks to the current GNSS velocity field, which is dense and updated, we can easily model far and near-fault with high accuracy.

7. M2000 is the most valuable data set to compare pre-1999 loading and the present. The profile NAF 11 (Figure 10) transects the epicentre of Mw 7.4 1999 İzmit earthquake, where the difference between pre-1999 fault-parallel velocity and the present value is ~6 mm/y. Özarpacı et al. (2021) showed that the creep rate is decreasing and has not yet reached a steady-state, as is the case for İsmetpasa. This might be related either to the fault healing process or partial locking below the creeping zone.

8. Profile 12 in Figure 10 marks the splitting zone of NAF in the Sea of the Marmara into the two branches (Northern and Southern segments). As the Sea of Marmara hinders GNSS observations here, we simplified this rather complicated zone with a single fault model. For convenience, this uncertain area is shaded in dark grey (Profile NAF 12, Figure 10) and estimated the total slip instead of focusing on the two branches in the near field. All three profiles crossing the Sea of Marmara yield slip-rates of 26 mm/yr (Figure 9, Profile NAF11-13), in agreement with Eurasia- Anatolia relative motion. This corroborates the earlier results that the Main Marmara Fault is responsible for accommodating the bulk of deformation and the faults in the south of the Sea of Marmara are not very active. Nevertheless, very low slip deficit rates do not preclude the occurrence of large earthquakes. Although our deduction is as good as the validity of the assumed 16 km locking depth, the choice of different locking depths does not result in significant changes in slip rates- as these values are well constrained (e.g., Wright et al. 2013).

9. Interestingly, the agreement of far-field data for M2000 and K2014 is outstanding. In Figure 10, the velocities predicted by M2000 and what we have solved in this study are very close to each other, especially in the fault-parallel velocities of the stations projecting to NAF12 and NAF13 profiles. In other words, there has been no change in fault-parallel velocities in the intervening 22 years. Whereas, the NAF zone is fanned out in the west and is a wide shear zone, with many small scale subparallel faults (Şengör et al. 2005). The absence of a significant velocity difference suggests the following interpretations:

a. the faults here are either completely locked or there are no active faults here.

b. If these faults are locked, this might mean that the deformations of the 1999 İzmit and Düzce events are not distributed on the secondary faults in Anatolia or the slip partitioning is within the standard deviation of our data (~1.5 mm/yr).

10. The deviation from a single fault model is apparent in the southern part of the NAF06 profile, with misfits on the order of 2–3 mm/yr. We think that this misfit may be an indication of the strain partitioning between the main NAF and its splays, especially the Sungurlu fault.

4.2. Implications for InSAR velocity field

Interferometric Synthetic Aperture Radar (InSAR) satellites revolve on a polar orbit and thus are insensitive to crustal motion with predominantly northerly motions. The transformation of line-of-sight displacement to a description in east, north, and up is an underdetermined inverse problem that requires constraining the N-component of the velocity field–this comes from the GNSS velocity fields. The difference between the N-component of the gridded velocities of Kreemer et al. (2014) and this study is given in Figure 7, where significant differences in the proximity of NAF and EAF suggest InSAR derived strain-rate field could be improved by using our solution (e.g., Weiss et al., 2020).

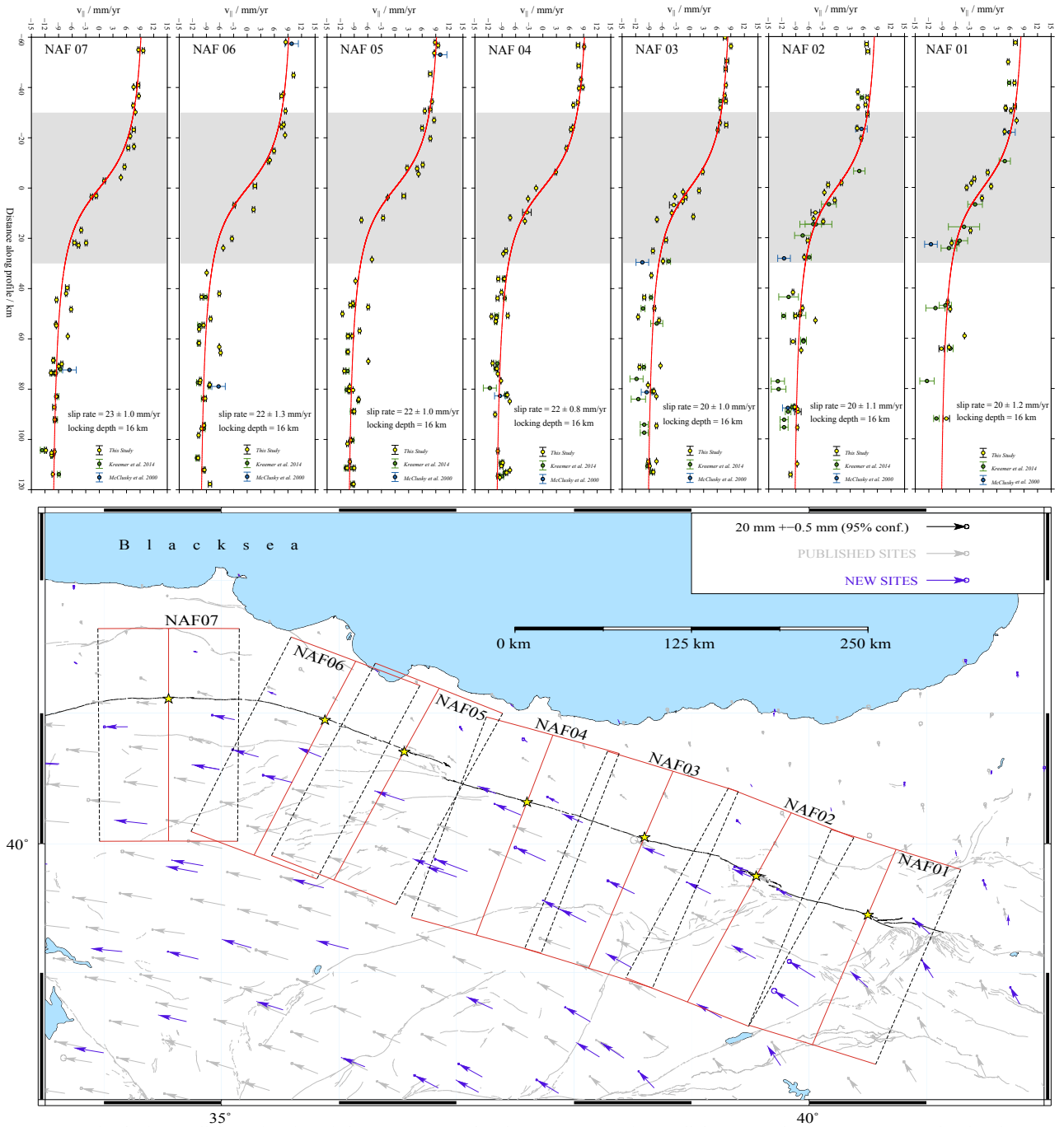

Figure 10. The fault-parallel (strike-slip) deformation rates for the NAF. (a) Fault-parallel GNSS velocities at a perpendicular distance from the surface trace of the fault at the midsection of each profile (solid circles) and the deformation expected for an infinitely long, vertical strike-slip fault in an elastic half-space for fixed (16 km) locking depth (red curves; Savage and Burford, 1973). The legend indicates the data sources and estimated model parameters. The axes scaling is fixed for facilitating comparison with the other plots. Inferred deformation zone related to strain loading is shaded in grey. The time series, which were recorded posterior to the publication of the sites shown in grey are all reprocessed. (b) Profile locations, and the active fault map of Turkey (Emre et al., 2013). Yellow stars mark the intersection of NAF with the profiles.

5. Conclusions

In this study, we derived a new velocity field from up to 28 years of campaign and continuous GNSS data, with an additional epoch at 186 campaign sites of Kurt et al. (2020). The velocity solutions are processed using unified processing for a single reference frame, allowing

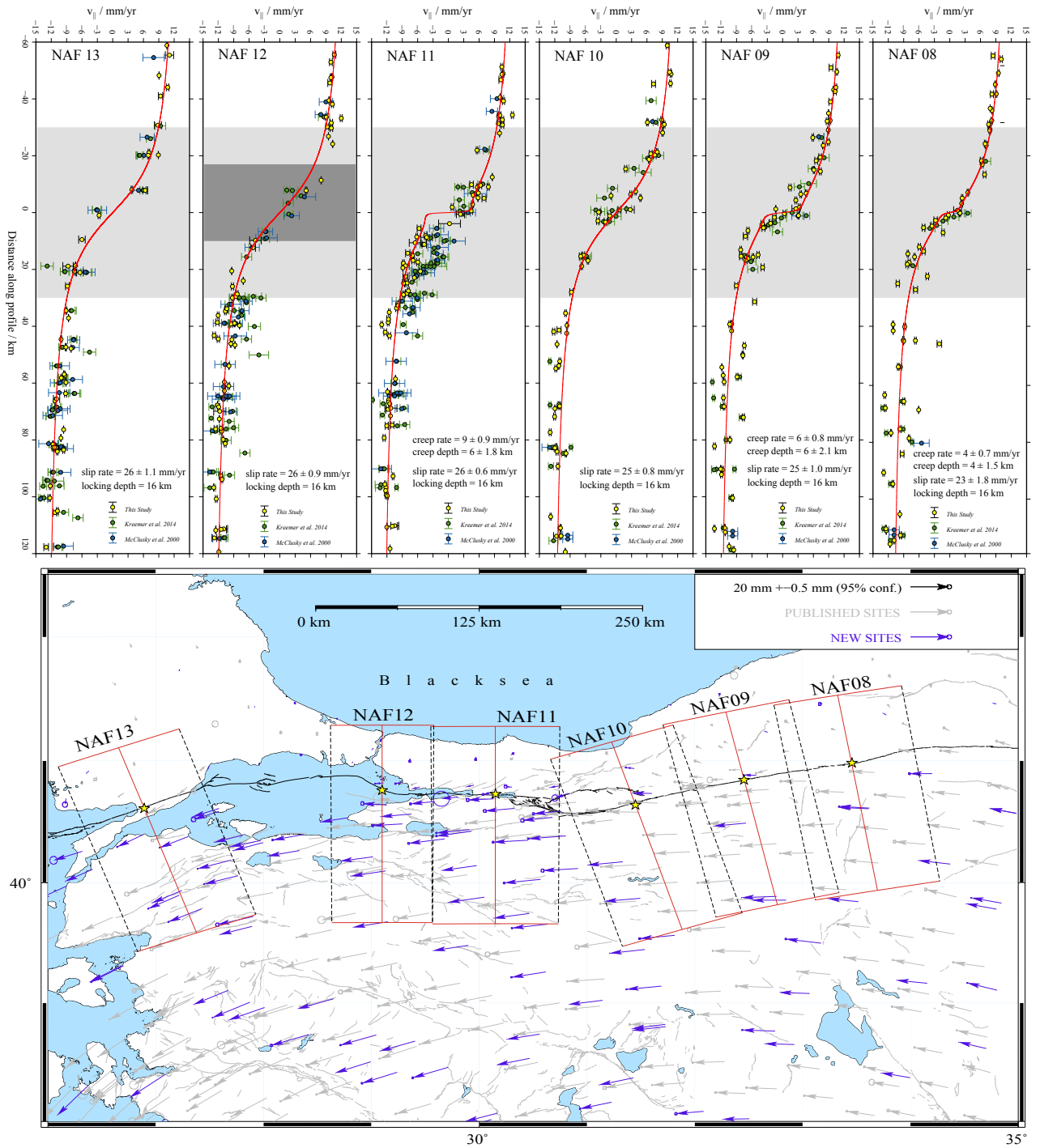

Figure 10. (Continued).

realistic uncertainties on the order of <1 mm/y. With this improvement, we report more precise estimates of strain accumulation along the NAF and EAF. Furthermore, the new observations we report should provide improved estimates of elastic dislocation parameters for secondary faults. We believe that an invaluable and up-to-date velocity field having unprecedented spatial coverage and resolution in this study will help researchers to understand the tectonic behavior and seismicity of Anatolia and surrounding regions.

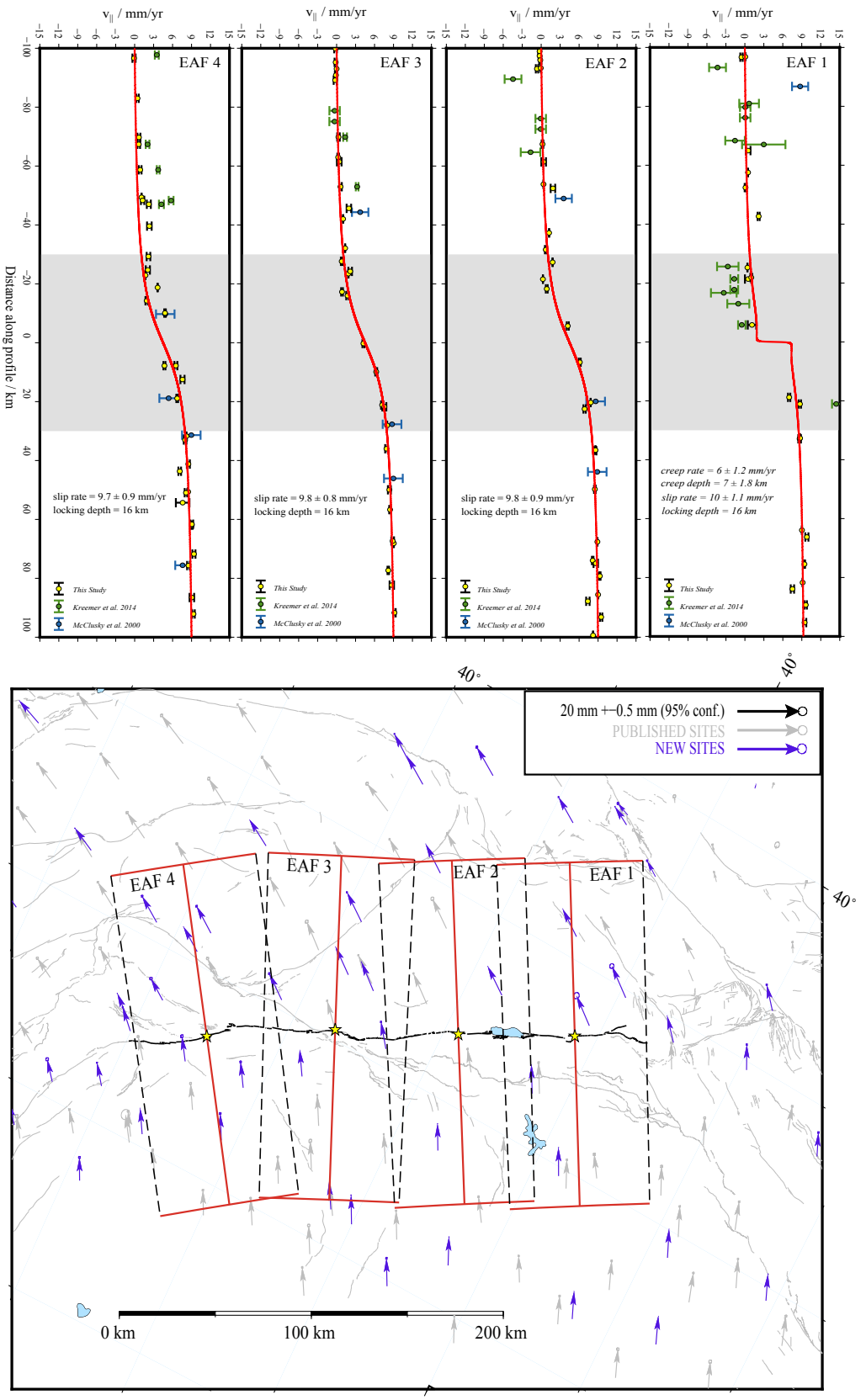

Figure 11. The fault-parallel (strike-slip) deformation rates for the EAF. The details are the same as in Figure 10.

Acknowledgements

Figures 3, 6, 10, 11 and the Supplementary Figures are produced by GMT software (Wessel et al., 2019). The Project Protocol (dated 05 October 2017) between the General Directorate of Mapping and Yıldız Technical University and researchers from Boğaziçi University Kandilli Observatory and Earthquake Research Institute made this research possible and is hereby acknowledged. The authors are grateful to Rob Reilinger and an anonymous referee for their comments and suggestions. We thank MAGNET, BUSKİ, SASKİ, İSKİ for providing time series for some of the stations included in this study. Finally, we thank all the personnel from the three parties who are involved in data collection which made these analyses possible.

Supplementary Data

Supplementary data can be accessed at the following link: https://aperta.ulakbim.gov.tr/record/252408#.ZF35yXZByUl

References

Aktuğ B, Kılıçoğlu A (2006). Recent crustal deformation of Izmir, Western Anatolia and surrounding regions as deduced from repeated GPS measurements and strain field. Journal of Geodynamics 41 (5): 471–484. https://doi.org/10.1016/j.jog.2006.01.004

Aktug B, Nocquet, JM, Cingöz A, Parsons B, Erkan Y et al. (2009a). Deformation of western Turkey from a combination of permanent and campaign GPS data: Limits to block-like behavior. Journal of Geophysical Research 114: B10404. https://doi.org/10.1029/2008JB006000

Aktuğ B, Kılıçoğlu A, Lenk O, Gürdal MA (2009b). Establishment of regional reference frames for detecting active deformation areas in Anatolia. Studia Geophysica et Geodaetica 2 (53): 169–183. https://doi.org/10.1007/s11200-009-0011-0

Aktuğ B, Sezer S, Özdemir S, Lenk O, Kılıçoğlu A (2011). Computation of the actual coordinates and velocities of Turkish national fundamental GPS network. Harita Dergisi 145: 1-14 (in Turkish)

Aktuğ B, Parmaksız E, Kurt M, Lenk O, Kılıçoğlu MA et al. (2013). Deformation of Central Anatolia: GPS implications. Journal of Geodynamics 67: 78-96. https://doi.org/10.1016/j.jog.2012.05.008

Aktuğ B, Doğru A, Özener H, Peyret M (2015). Slip rates and locking depth variation along central and easternmost segments of North Anatolian Fault. Geophysical Journal International 202 (3): 2133–2149. https://doi.org/10.1093/gji/ggv274

Aktug B, Ozener H, Dogru A, Sabuncu A, Turgut B et al. (2016). Slip rates and seismic potential on the East Anatolian Fault System using an improved GPS velocity field. Journal of Geodynamics 94–95: 1-12. https://doi.org/10.1016/j.jog.2016.01.001

Altamimi Z, Rebischung P, Métivier L, Collilieux X (2016). ITRF2014: A new release of the International Terrestrial Reference Frame modeling nonlinear station motions. Journal of Geophysical Research 121: 6109–6131. https://doi.org/10.1002/2016JB013098

Altamimi Z, Métivier L, Rebischung P, Rouby H, Collilieux X (2017). ITRF2014 plate motion model. Geophysical Journal International 209 (3): 1906–1912. https://doi.org/10.1093/gji/ggx136

Aslan G, Lasserre C, Çakir Z, Ergintav S, Özarpaci S et al. (2019). Shallow creep along the 1999 Izmit Earthquake rupture (Turkey) from GPS and high temporal resolution interferometric synthetic aperture radar data (2011–2017). Journal of Geophysical Research 124 (2): 2218-2236. https://doi.org/10.1029/2018JB017022

Avouac J-P (2015). From geodetic imaging of seismic and aseismic fault slip to dynamic modeling of the seismic cycle. Annual Review of Earth and Planetary Sciences 43: 233-271. https://doi.org/10.1146/annurev-earth-060614-105302

Ayhan ME, Demir C, Lenk O, Kılıçoğlu A, Aktuğ B et al. (2002a). Turkish national fundamental GPS network -1999A (TFGN-99A). Harita Dergisi, Special Publication 16 (in Turkish).

Ayhan ME, Demir C, Lenk O, Kilicoglu A, Altiner Y et al. (2002). Interseismic strain accumulation in the Marmara Sea region, Bulletin of the Seismological Society of America 92 (1): 216–229. https://doi.org/10.1785/0120000818

Bilham R, Ozener H, Mencin D, Dogru A, Ergintav S et al. (2016). Surface creep on the North Anatolian Fault at Ismetpasa, Turkey, 1944–2016. Journal of Geophysical Research 121 (10): 7409-7431. https://doi.org/10.1002/2016JB013394

Bird P, Jackson DD, Kagan YY, Kreemer C, Stein RS (2015). GEAR1: A global earthquake activity rate model constructed from geodetic strain rates and smoothed seismicity. Bulletin of the Seismological Society of America 105 (5): 2538-2554. https://doi.org/10.1785/0120150058

Bletery Q, Cavalié O, Nocquet JM, Ragon T (2020). Distribution of interseismic coupling along the North and East Anatolian Faults inferred from InSAR and GPS data. Geophysical Research Letters 47 (16): e2020GL087775. https://doi.org/10.1029/2020GL087775

Blewitt G, Lavallee D (2002). Effect of Annual Signals on Geodetic Velocity. Journal of Geophysical Research 107 (B7). https://doi.org/10.1029/2001JB000570

Cakir Z, Akoglu AM, Belabbes S, Ergintav S, Meghraoui M (2005). Creeping along the Ismetpasa section of the North Anatolian fault (Western Turkey): Rate and extent from InSAR. Earth and Planetary Science Letters 238 (1-2): 225-234. https://doi.org/10.1016/j.epsl.2005.06.044

Çakir Z, Ergintav S, Özener H, Dogan U, Akoglu AM et al. (2012). Onset of aseismic creep on major strike-slip faults. Geology 40 (12): 1115-1118. https://doi.org/10.1130/G33522.1

Cakir Z., Ergintav S, Akoğlu AM, Çakmak R, Tatar O et al. (2014). InSAR velocity field across the North Anatolian Fault (eastern Turkey): Implications for the loading and release of interseismic strain accumulation. Journal of Geophysical Research 119 (10): 7934-7943. https://doi.org/10.1002/2014JB011360

Cavalié O, Jónsson S (2014). Block-like plate movements in eastern Anatolia observed by InSAR. Geophysical Research Letters 41 (1): 26-31. https://doi.org/10.1002/2013GL058170

Cetin E, Cakir Z, Meghraoui M, Ergintav S, Akoglu AM (2014). Extent and distribution of aseismic slip on the Ismetpaşa segment of the North Anatolian Fault (Turkey) from Persistent Scatterer InSAR. Geochemistry, Geophysics, Geosystems 15 (7): 2883-2894. https://doi.org/10.1002/2014GC005307

Dogru A, Gorgun E, Ozener H, Aktug B (2014). Geodetic and seismological investigation of crustal deformation near Izmir (western Anatolia). Journal of Asian Earth Sciences 82: 21–31. https://doi.org/10.1016/j.jseaes.2013.12.008

Emre Ö, Duman T, Özalp S, Elmacı H, Olgun Ş et al. (2013). Açıklamalı Türkiye Diri Fay Haritası. Ölçek 1:1.250.000, Maden Tetkik ve Arama Genel Müdürlüğü, Özel Yayın Serisi 30, Ankara, ISBN: 978-605- 5310-56-1 (in Turkish)

Ergintav S, Reilinger RE, Çakmak R, Floyd M, Cakir Z et al. (2014). Istanbul's earthquake hot spots: Geodetic constraints on strain accumulation along faults in the Marmara seismic gap. Geophysical Research Letters 41: 5783–5788. https://doi.org/10.1002/2014GL060985

Faccenna C, Becker TW (2010). Shaping mobile belts by small-scale convection. Nature 465: 602-605. https://doi.org/10.1038/nature09064

Güvercin SE, Karabulut H, Konca AÖ, Doğan U, Ergintav S (2022). Active Seismotectonics of the East Anatolian Fault. Geophysical Journal International 230 (1): 50–69. https://doi.org/10.1093/gji/ggac045

Haines AJ, Dimitrova LL, Wallace LM, Williams CA (2015). Enhanced surface imaging of crustal deformation: Obtaining tectonic force fields using GPS data. New York, U.S.A: Springer. https://doi.org/10.1007/978-3-319-21578-5

Herring TA, King RW, Floyd MA, McClusky SC (2018). GAMIT Reference Manual, GPS Analysis at MIT, Release 10.7, http://geoweb.mit.edu/gg/GAMIT_Ref.pdf.

Kreemer C, Lavallée DA, Blewitt G, Holt WE (2006). On the stability of a geodetic no-net-rotation frame and its implication for the International Terrestrial Reference Frame. Geophysical Research Lettetter 33: L17306. https://doi.org/10.1029/2006GL027058

Kreemer C, Blewitt G, Klein EC (2014). A geodetic plate motion and Global Strain Rate Model. Geochemistry, Geophysics, Geosystems 15 (10): 3849-3889. https://doi.org/10.1002/2014GC005407

Kurt Aİ, Cingöz A, Özdemir S, Peker S, Özel Ö et al. (2020). Estimation of the Updated Coordinates and Velocities of Turkish National Fundamental GNSS Network within the Context of GNSS Data Reprocessing. Harita Dergisi 164: 1-17 (in Turkish).

Mahmoud Y, Masson F, Meghraoui M, Cakir Z, Alchalbi A et al. (2013). Kinematic study at the junction of the East Anatolian fault and the Dead Sea fault from GPS measurements. Journal of Geodynamics 67: 30-39. https://doi.org/10.1016/j.jog.2012.05.006

McClusky S, Balassanian S, Barka A, Demir C, Ergintav S et al. (2000). Global Positioning System constraints on plate kinematics and dynamics in the eastern Mediterranean and Caucasus. Journal of Geophysical Research 105 (B3): 5695–5719. https://doi.org/10.1029/1999JB900351

Nocquet JM (2012). Present-day kinematics of the Mediterranean: A comprehensive overview of GPS results. Tectonophysics 579: 220-242. https://doi.org/10.1016/j.tecto.2012.03.037

Ozener H, Arpat E, Ergintav S, Dogru A, Cakmak R et al. (2010). Kinematics of the eastern part of the North Anatolian Fault Zone. Journal of Geodynamics 49 (3-4): 141–150. https://doi.org/10.1016/j.jog.2010.01.003

Ozener H, Yilmaz O, Dogru A, Turgut B, Gurkan O (2013a). GPS-derived velocity field of the Iznik-Mekece segment of the North Anatolian Fault Zone. Journal of Geodynamics 67: 46–52. https://doi.org/10.1016/j.jog.2012.07.001

Ozener H, Dogru A, Acar M (2013b). Determination of the displacements along the Tuzla Fault (Aegean region-Turkey): preliminary results from GPS and precise leveling techniques. Journal of Geodynamics 67: 13–20. https://doi.org/10.1016/j.jog.2012.06.001

Ozener H, Dogru A, Turgut B (2013c). Quantifying aseismic creep on the Ismetpasa segment of the North Anatolian Fault Zone (Turkey) by 6 years of GPS observations. Journal of Geodynamics 67:72-77. https://doi.org/10.1016/j.jog.2012.08.002

Özarpacı S, Doğan U, Ergintav S, Çakır Z, Özdemir A, et al. (2021). Present GPS velocity field along 1999 Izmit rupture zone: evidence for continuing afterslip 20 yr after the earthquake. Geophysical Journal International 224 (3): 2016-2027. https://doi.org/10.1093/gji/ggaa560.

Özbakır AD, Govers R, Wortel R (2017). Active faults in the Anatolian-Aegean plate boundary region with Nubia. Turkish Journal of Earth Sciences 26 (1): 30-56. https://doi.org/10.3906/yer-1603-4

Özbey V, Özeren MS, Henry P, Klein E, Galgana G et al. (2021). Kinematics of the Marmara Region: a fusion of continuum and block models. Mediterranean Geosciences Reviews 3: 57-78. https://doi.org/10.1007/s42990-021-00051-y

Özeren, M.S., Holt, W.E. (2010) The dynamics of the eastern Mediterranean and eastern Turkey. *Geophysical Journal International* 183: 1165–1184. https://doi.org/10.1111/j.1365-246X.2010.04819.x

Reilinger RE, McClusky S, Vernant P, Lawrence S, Ergintav S et al. (2006). GPS constraints on continental deformation in Africa–Arabia–Eurasia continental collision zone and implications for the dynamics of plate interactions. Journal of Geophysical Research 111 (B5): B05411. https://doi.org/10.1029/2005JB004051

Reilinger RE, McClusky S (2011). Nubia–Arabia–Eurasia plate motions and the dynamics of Mediterranean and Middle East tectonics. Geophysical Journal International 186 (3): 971–979. https://doi.org/10.1111/j.1365-246X.2011.05133.x

Savage JC, Burford RO (1973). Geodetic determination of relative plate motion in central California. Journal of Geophysical Research 78 (5): 832-845. https://doi.org/10.1029/JB078i005p00832

Smith-Konter BR, Sandwell DT, Shearer P (2011). Locking depths estimated from geodesy and seismology along the San Andreas Fault System: Implications for seismic moment release. Journal of Geophysical Research 116 (B6). https://doi.org/10.1029/2010JB008117

Şengör AMC, Tüysüz O, Imren C, Sakınç M, Eyidoğan H et al. (2005). The North Anatolian fault: A new look. Annual Reviews of Earth and Planetary Science Letters 33: 37-112. https://doi.org/10.1146/annurev.earth.32.101802.120415

Tan O (2021). A homogeneous earthquake catalogue for Turkey. Natural Hazards and Earth System Sciences 21 (7): 2059-2073. https://doi.org/10.5194/nhess-21-2059-2021

Tatar O, Poyraz F, Gürsoy H, Cakir Z, Ergintav S et al. (2012). Crustal deformation and kinematics of the Eastern Part of the North Anatolian Fault Zone (Turkey) from GPS measurements. Tectonophysics 518-521: 55–62. https://doi.org/10.1016/j.tecto.2011.11.010

Thatcher W (2009). How the Continents Deform: The Evidence From Tectonic Geodesy. Annual Review of Earth and Planetary Sciences 37: 237-262. https://doi.org/10.1146/annurev.earth.031208.100035

Tiryakioğlu İ, Floyd M, Erdogan S, Gülal E, Ergintav S et al. (2013). GPS constraints on active deformation in the Isparta Angle region of SW Turkey. Geophysical Journal International 195 (3): 1455–1463. https://doi.org/10.1093/gji/ggt323

Vernant P. (2015). What can we learn from 20 years of interseismic GPS measurements across strike-slip faults? Tectonophysics 644: 22-39. https://doi.org/10.1016/j.tecto.2015.01.013

Walters RJ, Parsons B, Wright TJ (2014). Constraining crustal velocity fields with InSAR for Eastern Turkey: Limits to the block-like behavior of Eastern Anatolia. Journal of Geophysical Research 119 (6): 5215-5234. https://doi.org/10.1002/2013JB010909

Wei M, Sandwell D, Smith-Konter B (2010). Optimal combination of InSAR and GPS for measuring interseismic crustal deformation. Advances in Space Research 46 (2): 236-249. https://doi.org/10.1016/j.asr.2010.03.013

Weiss JR, Walters RJ, Morishita Y, Wright TJ, Lazecky M et al. (2020). High-resolution surface velocities and strain for Anatolia from Sentinel-1 InSAR and GNSS data. Geophysical Research Letters 47 (17): e2020GL087376. https://doi.org/10.1029/2020GL087376

Wessel P, Luis JF, Uieda L, Scharroo R, Wobbe F et al. (2019). The Generic Mapping Tools version 6. Geochemistry, Geophysics, Geosystems 20: 5556-5564. https://doi.org/10.1029/2019GC008515

Wright TJ., Elliott JR, Wang H, Ryder I (2013). Earthquake cycle deformation and the Moho: Implications for the rheology of continental lithosphere. Tectonophysics 609: 504-523. https://doi.org/10.1016/j.tecto.2013.07.029

Yavaşoğlu H, Tarı E, Tüysüz O, Çakır Z, Ergintav S (2011). Determining and modeling tectonic movements along the central part of the North Anatolian Fault (Turkey) using geodetic measurements. Journal of Geodynamics 51 (5): 339–343. https://doi.org/10.1016/j.jog.2010.07.003.